Two-laser dynamic nuclear polarization with semiconductor electrons: Feedback, suppressed fluctuations, and bistability near two-photon resonance

A. R. Onur* and C. H. van der Wal
Zernike Institute for Advanced Materials, University of Groningen, 9747AG Groningen, The Netherlands

(Received 7 August 2018; published 11 October 2018)

Feedback control is a powerful tool to stabilize systems for which precision control is difficult to impose directly, such as the environment of an open quantum system. Reduction of noise from the environment is a major challenge on the road to harnessing delicate quantum effects such as superposition and entanglement. In particular, spin states of defects and quantum dots in semiconductors display promising coherence properties for future applications, often being limited by disturbance from disordered nuclear spins in their environment. Here we show how optical coherent population trapping (CPT) of the spin of localized semiconductor electrons stabilizes the surrounding nuclear spins via feedback control. We find distinct control regimes for different signs of laser detuning and examine the transition from an unpolarized, narrowed state to a polarized state possessing a bistability. The narrowing of the state protects the electron spin against dephasing and yields self-improving CPT. Our analysis is relevant for a variety of solid-state systems where hyperfine-induced dephasing is a limitation for using electron spin coherence.

DOI: 10.1103/PhysRevB.98.165304

I. INTRODUCTION

A localized electron spin coupled to nuclear spins in a solid allows for studying the dynamics of mesoscopic spin ensembles. It forms a realization of the Gaudin (central spin) model [1] with the number of spins ranging from $\sim$10–10^6. From an application perspective the isolated dynamics of the electron spin is interesting as it can be used for quantum information processing. In thermal equilibrium the nuclear spins act as a source of dephasing for the electron spin. Optical orientation of the electron spin can be used to prepare out-of-equilibrium nuclear spin states via dynamic nuclear polarization (DNP) [2–4]. In turn, polarized nuclear spins induce an energy shift for the electron spin states, which can be described as an effective magnetic (Overhauser) field. DNP can also reduce thermal fluctuations in the nuclear spin polarization, which increases the electron spin dephasing time. This can be done either by creating a large nuclear spin polarization or by squeezing the polarization into a narrowed distribution [5,6]. Significant achievements have been made for both cases via electron transport, electron spin resonance, and optical preparation techniques [4,7–17]. We present here how optical coherent population trapping (CPT) of localized semiconductor electrons [18] stabilizes the surrounding nuclear spin bath in a state which is more ordered than the thermal equilibrium state.

CPT is the phenomenon where two-laser driving from the electron spin states to a common optically excited state displays—on exact two-photon resonance—a suppression of optical excitation due to destructive quantum interference in the dynamics [19], and is a key effect in quantum information processing [20]. Its sharp spectral feature allows for highly selective control over absorption and spontaneous emission of light. With atoms this has been applied in selective Doppler and sideband cooling [21–23]. Similarly, in semiconductors the CPT resonance can selectively address localized electrons that experience a particular Overhauser field [24–26]. This can lead to trapping of the combined electron-nuclear spin system in a dark state which was demonstrated as a measurement-based technique for reducing uncertainty of the nuclear spin state around a nitrogen vacancy center [15].

The CPT-based control scheme we propose relies on an autonomous feedback loop, existing for detuned lasers only, and does not require measurement or adaptation of control lasers [24]. Earlier work found such a feedback loop in an effective two-level description of a driven three-level Λ system [26]. We use a full description of the Λ system dynamics, uncover distinct control regimes for different signs of the detuning, and examine the transition from an unpolarized, narrowed state for blue-detuned lasers to a polarized state possessing a bistability for red-detuned lasers. With a stochastic approach that was previously used in the context of electron spin resonance experiments [11,27] we analyze the evolution of thermalized nuclear spins to a state of reduced entropy. Our method thus expands the established CPT technique for coherent electron spin preparation and manipulation [28] to one that can also improve the electron spin dephasing time by nuclear spin preparation.

The model applies to a class of localized systems that are characterized by low strain and spherical symmetry of the confining potential. For these the hyperfine interaction between the nuclear spins and the hole of the optically excited state is an order of magnitude smaller than the electron [29] and we consider it negligible. The stabilization of the nuclear spin bath purely arises from DNP mediated by the hyperfine interaction for the ground-state electron [30,31]. Prerequisites

*Now at Department of Medical Technology and Clinical Physics, University Medical Center Utrecht, 3584CX Utrecht, The Netherlands; a.r.onur@gmail.com

are a high nuclear spin temperature and a nonzero electron spin temperature (ensuring bidirectional DNP). We focus our analysis on the case of the donor-bound electron in GaAs, which has these properties, and in our example calculations use parameters that approach (in order of magnitude) values that apply to this system [4]. We expect this work to also be applicable to strain-free quantum dots [32] and other solid-state spin defects where the hyperfine contact interaction for the electron is dominant. Our analysis differs from nuclear spin stabilization demonstrated in self-assembled quantum dots [12,33] where hole-mediated DNP does contribute due to the design of these structures: a noncollinear hole-nuclear spin coupling [34,35] arises due to anisotropy [36], and lattice strain results in a noncollinear interaction between the electron and nuclear spin [37]. We predict different features than [12] and discuss how these are distinguishable in experiment. In parallel with this theoretical work, our team explored the validity of our model with experiments on donor-bound electrons in GaAs, and observed its key fingerprints [38].

II. CPT WITH LASER AND OVERHAUSER DETUNINGS

Figure 1(a) presents the electronic part of our model: a Λ system with spin states $|1\rangle$ and $|2\rangle$ that each have an optical transition to state $|3\rangle$. Nuclear spin polarization gives an Overhauser shift $-(+)\hbar\delta$ of the state $|1\rangle$ ($|2\rangle$), and we assume the Overhauser shift of $|3\rangle$ to be negligible. The values of energy differences $\hbar\omega_{13}$ and $\hbar\omega_{23}$ and Zeeman splitting $\hbar\omega_z$ between these states are defined for $\delta = 0$. Two laser fields with frequencies ω_1 and ω_2 (and Rabi frequencies Ω_1 and Ω_2) selectively drive the two transitions.

The decay and decoherence rates of the system are the spin flip rate Γ_s, excited-state decay rate Γ_3, spin decoherence rate γ_s, and excited-state decoherence rate γ_3. We take all decay rates symmetric for the two electron spin states (for Γ_s this implies temperature $k_B T \gg \hbar\omega_z$), to avoid needless complication of the discussion, but our conclusions remain valid for the nonsymmetric case. For modeling the CPT effects we directly follow Ref. [20]. Appendix A 1 specifies this in our notation. For this system, CPT occurs for driving at two-photon resonance (TPR; i.e., for $\delta = 0$, $\omega_1 = \omega_2 + \omega_z$). In the conventional picture of CPT, one laser is fixed at single laser detuning Δ while the other is scanned across the resonance. At the TPR point the system shows reduced absorption, getting trapped in a dark state that equals (for ideal spin coherence) $|\Psi\rangle \propto \Omega_2 |1\rangle - \Omega_1 |2\rangle$. Figure 1(b) presents this for different Δ in terms of the system's steady-state density-matrix element ρ_{13}.

For our DNP analysis, however, we study CPT as a function of δ while the two lasers are fixed to exact TPR for $\delta = 0$. This is the electron's point of view on how a finite Overhauser shift breaks the ideal CPT condition, and the dependence on δ reflects the sharp spectral CPT feature. Figure 1(c) presents how this works out for the electron spin polarization, $(\rho_{22} - \rho_{11})/2$, in terms of the steady-state density matrix. The effect of a nonzero Overhauser shift is to break the TPR setting of the lasers [the detuning of laser 1 (2) from its corresponding transition is then $\Delta - (+)\,\delta$]. For $\Delta = 0$ this has no effect on the spin polarization since δ drives both lasers away from resonance by an equal amount. For finite Δ, however, the

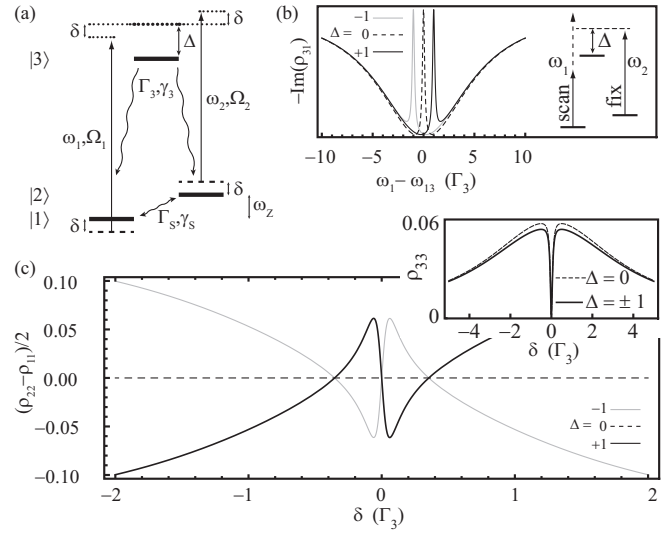

FIG. 1. Electronic level scheme and response under two-laser driving. (a) Schematic of energies and shifts of the electronic three-level system (for brevity the figure omits factors $\hbar$). Thick black lines are the (not Overhauser shifted) spin states $|1\rangle$, $|2\rangle$ and optically excited state $|3\rangle$, with energy splittings ω_{13}, ω_{23}, and ω_z. Γ_s, γ_s and Γ_3, γ_3 are spin- and excited-state decay and decoherence rates, respectively. Two lasers (frequencies ω_1 and ω_2) couple to the system with Rabi frequencies Ω_1 and Ω_2, excited-state detuning Δ, and Overhauser shift δ (see further main text). (b) Conventional depiction of CPT (here for $\delta = 0$ Overhauser shift) showing the narrow CPT resonance within a broader absorption line. Laser 1 scans over the resonance while laser 2 is held fixed at $\omega_2 = \omega_{23} + \Delta$, for detunings Δ as labeled. (c) Electron spin polarization as a function of Overhauser shift δ, with lasers fixed at $\omega_1 = \omega_{13} + \Delta$ and $\omega_2 = \omega_{23} + \Delta$. Inset: Excited-state population as a function of Overhauser shift (same parameters as main panel). In (b) and (c) results are presented as elements ρ_{ij} of the steady-state density matrix. All parameters are normalized with respect to $\Gamma_3 \equiv 1$: $\gamma_3 = 10$, $\Gamma_s = 10^{-4}$, $\gamma_s = 10^{-3}$, $\Omega_1 = \Omega_2 = 0.5$.

Overhauser shift leads to uneven detunings from the excited state, resulting in the electron spin polarization changing rapidly as a function of δ near TPR. Moreover, the electron spin polarization acquires a sign change as the sign of Δ is reversed. Notably, the excited-state population (ρ_{33}, inset) is symmetric with respect to the sign of Δ, which distinguishes the feedback mechanism that we discuss from mechanisms that depend on the excited-state population (as described in [12]). It is also interesting to observe that for $|\delta| \gtrsim 0.4$ the spin polarization has the sign which is expected for standard optical pumping (the population is transferred out of the spin state associated with the more resonant laser), while close to TPR it has the opposite sign (see Appendix B).

III. STABLE POINTS OF THE DRIVEN ELECTRON-NUCLEAR SPIN SYSTEM

How this electron spin polarization as a function of δ drives DNP (which in turn will influence δ) is the core of our further analysis. To this end, we consider the Λ system to be embedded in the crystal lattice where it couples to nuclear spins within the electron wave function. We study the combined

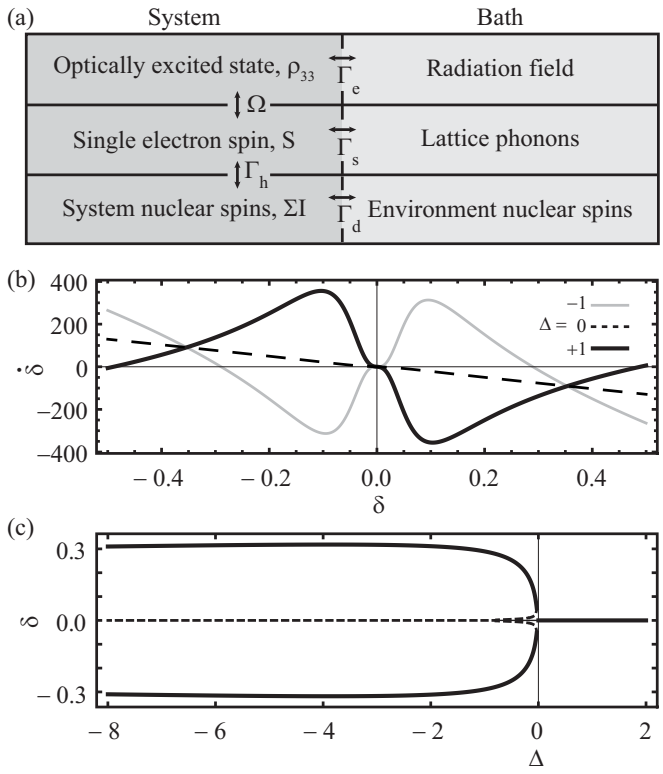

FIG. 2. Open system schematic, response function, and transition between distinct control regimes. (a) Overview of components and interactions of the laser-driven electron–nuclear-spin-ensemble system, with for each component its relaxation bath. Competition between the interactions and relaxation mechanisms govern the dynamics of the full system; see main text for details. (b) The rate $\dot{\delta}$ as a function of the Overhauser shift δ [Eq. (2)] that is experienced by the electron near CPT conditions, for detunings Δ as labeled and $\overline{\Gamma}_h/\Gamma_d = 0.01$. (c) Thick solid (dashed) lines display the one or two (un)stable stationary δ values ($\dot{\delta} = 0$) as a function of laser detuning Δ. The relaxation parameters and laser powers for (b) and (c) equal those of Fig. 1.

dynamics of the driven Λ system and its surrounding nuclear spin bath, and also take into account that this nuclear spin bath in turn couples to other nuclear spins of the crystal that are not in contact with the electron, leading to leakage of nuclear spin polarization by spin diffusion [Fig. 2(a)].

We first introduce relevant aspects of this hyperfine interaction. We concentrate on the common scenario where an external magnetic field is applied which defines a quantization axis for the spins, which we label $\hat{\mathbf{z}}$. This suppresses nonsecular (not energy conserving) terms in the nuclear spin dipole-dipole interaction and we can approximate the nuclear spins to be frozen on the timescale of electron spin dynamics [39–41]. The hyperfine Hamiltonian has electron-nuclear flip-flop terms that describe the transfer of spin angular momentum along $\hat{\mathbf{z}}$ between the two systems (Appendix A 2 provides a summary in our notation). For a single nuclear spin coupled to an electron, treated perturbatively, this results in the relaxation equation [42]

$$\langle \dot{I}_z \rangle = -\Gamma_h \left(\langle I_z \rangle - \langle \overline{I_z} \rangle - \frac{I^2 + I}{S^2 + S} [\langle S_z \rangle - \langle \overline{S_z} \rangle] \right). \quad (1)$$

Here I and I_z are the nuclear spin quantum number and spin component along $\hat{\mathbf{z}}$, and similarly for electron spin S. The overbar indicates that the expectation value is taken at thermal equilibrium. The effective hyperfine relaxation rate Γ_h is proportional to $\tau_c/(1 + \omega_z^2 \tau_c^2)$, which reflects how the electron spin correlation time τ_c determines the spectral density of the fluctuating hyperfine coupling [43]. The nuclear spin flips along $\hat{z}$ are allowed due to fluctuations in the electron spin component perpendicular to $\hat{z}$. These happen on the order of the intrinsic electron spin coherence time T_2 due to coupling to the crystal lattice. Additionally it is influenced by laser excitation because the repeated absorption and spontaneous emission also randomize the in-plane component of the electron spin. Thus the quenching of optical excitation due to CPT near $\delta = 0$ has an influence on Γ_h. In our model we take this into account by modulating the equilibrium hyperfine interaction rate $\overline{\Gamma}_h$ with the optical excitation rate obtained from the driven Λ-system dynamics of Fig. 1 (see Appendix A 3). Equation (1) shows that $\langle I_z \rangle$ can be controlled by bringing the electron spin out of thermal equilibrium. By summing Eq. (1) over all nuclei we can express the rate of change of δ as a function of δ, forming a closed-loop system, which includes the dependence on the out-of-equilibrium electron spin polarization,

$$\dot{\delta} = -\Gamma_h [\delta - K \langle S_z \rangle] - \Gamma_d \delta, \quad (2)$$

where K is a constant determined by the strength of the hyperfine coupling (see Appendix A 2) and we used again the high-temperature approximation $\langle \overline{S_z} \rangle = \overline{\langle \delta \rangle} = 0$. The last term of Eq. (2) incorporates the loss of nuclear spin polarization by diffusion to the environment at a rate Γ_d which we assume constant.

The polarization of the nuclear spin system is governed by the control dynamics of Eq. (2). It is an autonomous differential equation, which has equilibria at $\dot{\delta} = 0$. The equilibria constitute stable points when $\frac{\partial \dot{\delta}}{\partial \delta} < 0$. These are points of interest since, as we will show in the next section, they constitute attractors for the nuclear spin polarization as it evolves over time. The dominant factor that determines the behavior near the stable points is the sign change of the electron spin population; this can be such that DNP drives the system either towards or away from the equilibrium point. The sign of the hyperfine coupling, incorporated through Eq. (1), and the asymmetry introduced by the detuning Δ determine which equilibrium points are stable. The dependence of this control on driving CPT for the electron is shown in Fig. 2(b). Inclusion of the hyperfine relaxation and spin diffusion rates make that the graphs becomes tilted and distorted as compared to Fig. 1(c). The deformation reflects the dependence of Γ_h on the optical excitation rate and that the DNP is in competition with the nuclear spin diffusion that tends to relax the nuclear spin bath towards thermal equilibrium. Equilibrium points for which $\frac{\partial \dot{\delta}}{\partial \delta} > 0$ are unstable since the DNP acts in a way to drive nuclear polarization away from these points. The dashed line represents the system driven by two lasers with $\Delta = 0$, and has strong similarity with thermal equilibrium (no laser driving) because the Overhauser shift δ does not lead to a change in the electron spin polarization [see also the dashed line in Fig. 1(c)]. The position of the

stable point is at $\langle\bar{\delta}\rangle$, which we assumed zero. When the lasers are tuned to TPR for $\delta = 0$, while having a finite detuning Δ, two qualitatively different control regimes emerge. For the red-detuned case $\Delta = -1$ there are two stable points at $\delta \approx \pm 0.3$, and the nuclear spin system will thus display a bistability. For the blue-detuned case $\Delta = +1$, however, there is again one stable point at $\delta = 0$. The transition between these two control regimes is shown in Fig. 2(c) where the thick black lines represent the stable point(s) for a range of detunings Δ. Even though the blue-detuned case displays the same stable point as the equilibrium case there is an enhanced response towards $\delta = 0$ for a region around this point. The effect of this gain becomes apparent when we study the stochastics of the nuclear spin polarization. Notably, the small plateaus in the traces of Fig. 2(b) at $\delta = 0$ are due to the CPT suppression of Γ_h.

IV. SUPPRESSION OF NUCLEAR SPIN FLUCTUATIONS

The stochastics of the nuclear spin polarization gives rise to the electron spin dephasing time that is observed in measurements, whether on an ensemble of Λ systems [38,44] or by repeated measurements on a single system [4]. In such cases each system experiences a different Overhauser shift, sampled from a probability distribution $P(\delta)$, and this directly translates into a distribution for the electron precession frequencies. This can be used to calculate the dephasing time T_2^*, indicating when information on the electron spin state has decayed to $1/e$ of its initial value (see Appendix A 5). The evolution of $P(\delta)$ under the control dynamics of Eq. (2) can be described by a Fokker-Planck equation [27,45], in the continuum limit where the number of nuclear spins $N \gg 1$,

$$\dot{P} = \frac{2}{N}\frac{\partial}{\partial\delta}\left(-\dot{\delta}P + \frac{\delta_{\max}^2}{N}\frac{\partial}{\partial\delta}[\Gamma_d + \Gamma_h]P\right). \tag{3}$$

(Note: The derivation of a Fokker Planck equation for the nuclear spin polarization can be found in chapter 3 of Ref. [45]. Our Eq. (3) is identical to their Eq. (3.7), with $\dot{P}$ expressed in terms of δ, Γ_d, and Γ_h.) Here N is the number of system nuclear spins and $\delta_{\max}$ is the Overhauser shift for complete nuclear spin polarization (for simplicity, we describe the dynamics in the approximation where N spins with $I = \frac{1}{2}$ couple to the electron with equal strength [4]). Without laser driving Eq. (2) gives $\dot{\delta} = -(\Gamma_d + \Gamma_h)\delta$ and the steady-state solution to Eq. (3) is a Gaussian with standard deviation $\sigma_\delta = \delta_{\max}/\sqrt{N}$, as expected in thermal equilibrium. With laser driving the control gain becomes nonlinear, as in Fig. 2(b), and we evaluate the steady-state solution $P_{ss}(\delta)$ numerically (see Appendix A 4). With Eq. (3) we can study the evolution of the initial thermalized distribution $\overline{P}(\delta)$ while laser control is imposed via Eq. (2). The initial distribution depends on N and $\delta_{\max}$. For our example calculations we take $N = 10^5$, $\delta_{\max} = 16.3$, and $K = 10\delta_{\max}/3$ (see Appendix A 2), representing the donor-bound electron in GaAs [44] which has $\Gamma_3 \approx 1$ GHz.

The evolution of $P(\delta)$ corresponding to the response functions from Fig. 2(b) is depicted in Figs. 3(a) and 3(b). For the blue-detuned case $P(\delta)$ gets narrowed and focuses around the single stable point $\delta = 0$. This distribution results in a prolonged electron spin dephasing time. For the red-detuned case $P(\delta)$ splits apart and in the steady state it is divided between two stable points, each displaying a narrowed distribution with respect to the initial state. During evolution the rate of change of $P(\delta)$ is at first lagging at $\delta = 0$, causing the central dip in the gray lines of Fig. 3(a) and the central peak in Fig. 3(b). This is due to the suppressed hyperfine relaxation rate Γ_h at CPT resonance. At long timescales this effect smooths out.

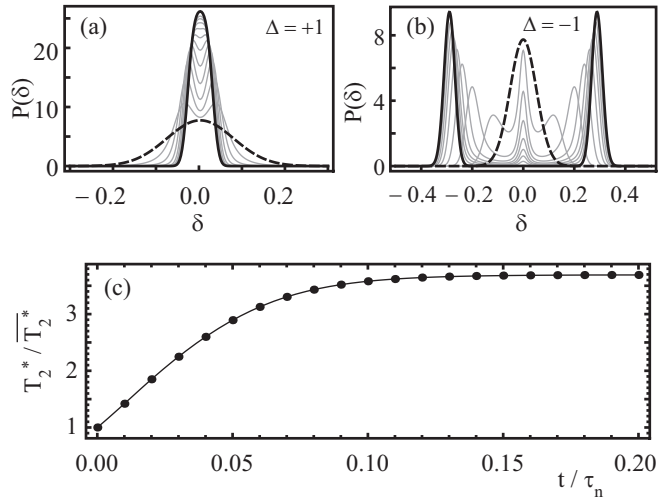

FIG. 3. Evolution of the nuclear spin polarization probability distribution. Time evolution of $P(\delta)$ for a nuclear spin bath with $N = 10^5$, for cases that correspond to the curves in Fig. 2(b), with $\Omega_1 = \Omega_2 = 0.5$ and $\overline{\Gamma}_h/\Gamma_d = 0.01$. In (a) and (b) the dashed lines show the same initial (Gaussian) distribution at thermal equilibrium (before laser driving is switched on); black lines show the final steady-state distribution. The sign of the detuning Δ determines whether the driven system has mono- or bistable behavior. Panel (c) shows the improvement in electron spin dephasing time corresponding to the sequence of curves in (a).

A thermodynamic interpretation of the narrowing effect is that when the driven Λ system is detuned from TPR, optical excitation converts low-entropy laser light to higher-entropy fluorescence light, resulting in an entropy flux away from the electron system. In turn, the electron acts as a controller on the nuclear spins, removing entropy from the spin bath and providing increased state information of the nuclear spins. Because of the slow dynamics of the nuclei this effect is sustained after laser control is turned off, giving an enhanced dephasing time for subsequent electron spin manipulation. The evolution of T_2^* calculated from $P(\delta)$ as in Fig. 3(a) is presented in Fig. 3(c), where the evolution time is expressed in units of the nuclear spin diffusion time $\tau_n = 1/\Gamma_d$ (on the order of seconds to minutes). The nuclear spin bath attains a stable state with an increase in T_2^* of a factor of $\sim$3.7 in $0.2\tau_n$. While this increase is moderate for the GaAs parameters used, it can be much more significant for systems with weaker nuclear spin diffusion (which can also be the case for GaAs when this is suppressed due to a Knight shift [38,46]). Notably, the resulting $P_{ss}(\delta)$ does not change with variation of $\overline{\Gamma}_h$ and Γ_d provided their ratio remains fixed. For the system nuclear spins this represents the ratio of coupling strength to the controller (electron spin) and the environment [Fig. 2(a)].

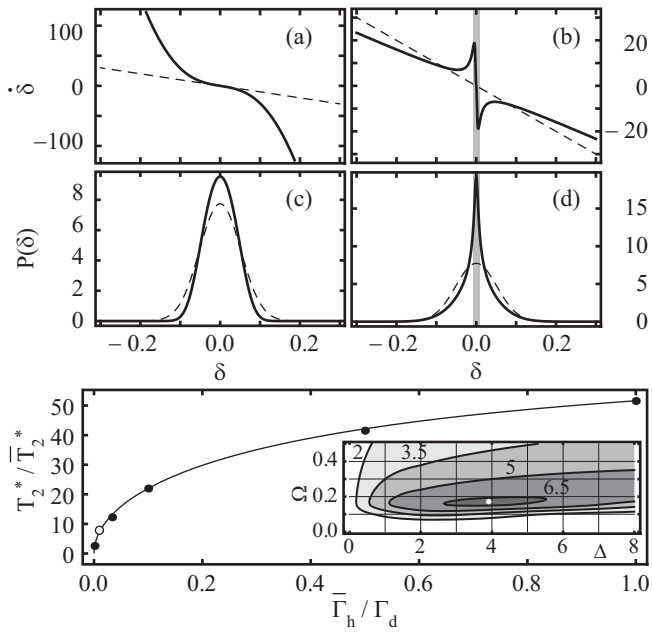

FIG. 4. Optimization of the T_2^* improvement factor and dependence on nuclear spin relaxation rates. Traces of driving rate $\dot{\delta}$ as a function of δ [black lines in panels (a) and (b)] and their respective effect on the nuclear spin distributions [(c) and (d)] for Rabi frequencies $\Omega = 2$ [(a) and (c)] and $\Omega = 0.1$ [(b) and (d)]. In (a) and (b) the dashed line is $\Gamma_d\delta$, representing the nuclear spin flip rate due to spin diffusion. In (c) and (d) the dashed line is the same (note different scale) nuclear spin probability distribution function at thermal equilibrium for $N = 10^5$ and $\overline{\Gamma}_h/\Gamma_d = 0.01$. The black line is the steady-state distribution under laser driving at detuning $\Delta = +1$ and Rabi frequencies $\Omega = 2$ (c) and $\Omega = 0.1$ (d). The gray area in (b) and (d) highlights the narrowing range. For low laser powers the driving curve (b) shows a steep response at $\delta = 0$ that acts as a strong force towards 0 for δ values around this point, and causes strong narrowing. The range over which narrowing takes place, however, is too small to cover the initial distribution. (e) Optimal T_2^* improvement as a function of $\overline{\Gamma}_h/\Gamma_d$. The simulated values (dots) reveal a dependence that scales with $[1/(1+\Gamma_d/\overline{\Gamma}_h)]^{1/2}$. Inset: Improvement factor in T_2^* for a range of detunings and laser powers at $\overline{\Gamma}_h/\Gamma_d = 0.01$. The white dot marks the optimum where $T_2^*/\overline{T}_2^* = 6.75$.

V. OPTIMAL DRIVING AND DEPENDENCE ON SYSTEM PARAMETERS

Figure 4 presents how the narrowing mechanism performs for different laser powers. At high power [Figs. 4(a) and 4(c); $\Omega_1 = \Omega_2 \equiv \Omega = 2$] the power broadening of the CPT resonance quenches the hyperfine rate Γ_h over a wide range around $\delta = 0$. This results in a weak response and the narrowing is only effective at the tails of the initial $P(\delta)$. At lower power [Figs. 4(b) and 4(d); $\Omega = 0.1$] there is a strong response around $\delta = 0$, indicating strong narrowing. However this does not extend far enough to include the tails of the initial $P(\delta)$. The T_2^* improvement factor in both cases is minor, only 1.38 and 1.63, respectively. Optimal T_2^* enhancement is found at moderate laser powers. Figure 4(e) depicts the optimum values as a function of $\overline{\Gamma}_h/\Gamma_d$. The inset shows how such an optimum is found from a map of $T_2^*/\overline{T}_2^*$ for a range of laser powers and detunings, for $\overline{\Gamma}_h/\Gamma_d = 0.01$ (open circle in main figure). These numerical results show that the optimal enhancement closely agrees with the square root dependence $T_2^*/\overline{T}_2^* \propto [1/(1+\Gamma_d/\overline{\Gamma}_h)]^{1/2}$. This reflects how, for the system nuclear spins, the ratio between the coupling to the electron and to the environment nuclear spins (giving rise to $\overline{\Gamma}_h$ and Γ_d, respectively) governs the optimal narrowing that can be achieved. This allows for estimating the maximal T_2^* enhancement in real solid-state spin systems, where spin diffusion always plays a role.

VI. DISCUSSION

In Ref. [12] a similar narrowing effect has been described and demonstrated for a quantum dot. The authors attribute it to the noncollinear hyperfine coupling for the hole spin in the optically excited state, while our result is based on electron-nuclear spin coupling. For paramagnetic defects, in general, either type of hyperfine coupling may dominate. To distinguish the two in experiment we point out two characteristics that are different and readily measurable. First, the transition from narrowing to a regime of bistability with changing sign of the detuning only occurs for our model. Second, the narrowing in Ref. [12] improves with increasing power while for our model there is a particular laser power that gives the optimal narrowing [Fig. 4(e)].

The effects we have discussed are readily measurable since, for blue detuning, the transmission of the laser beams tuned centrally on a narrow CPT line increases when the electron spin dephasing time increases. Hence, the narrowing of the nuclear spin polarization distribution directly translates to enhanced laser transmission over time (or equivalently, in a reduced signal when detecting fluorescence) and as such comprises a self-improving CPT effect. During the preparation of this paper our group has observed the bistability in the nuclear spin bath at silicon donors in GaAs [38]. Furthermore, in Ref. [47] it was demonstrated that the CPT-driven nuclear spin narrowing, and hence improvement of T_2^*, can be achieved in a single InGaAs quantum dot. These authors reported a 10-fold increase in T_2^*, which is slightly higher than our calculated optimum value of 6.75 based on parameters for Si-doped GaAs. A difference between dots and impurities can arise from the fact that the former have a material boundary, which suppresses spin diffusion. Also interestingly, they attribute the effect in their system to hyperfine interaction mediated by quadrupolar moments of the nuclei (which couple to electric field gradients present in the strained environment of the dot), whereas we took the Fermi contact hyperfine coupling as a starting point for our analysis, which we expect to dominate at strain-free impurities (and as already mentioned Ref. [12] attribute a similar effect to a hole spin-mediated hyperfine coupling). From such demonstrations we expect that the method described here is widely applicable to single-electron systems coupled by hyperfine interaction to a nuclear spin bath. And with each system having unique parameters for hyperfine coupling strength and spin diffusion, it would be interesting to see the technique applied to a wider range of impurities and quantum dots. Besides improving the coherence time of spin qubits for quantum information processing, the capability to prepare well-defined out-of-equilibrium states of the nuclear

spin bath in this way can give new insights into the nature of the electron-nuclear spin coupling and nuclear spin relaxation in these systems.

ACKNOWLEDGMENTS

We thank D. O'Shea, J. P. de Jong, J. Sloot, and A. U. Chaubal for valuable discussions, and acknowledge financial support from an ERC Starting Grant (Project No. 279931) and the Netherlands Organisation for Scientific Research (NWO, Project No. FOM-10PR2758).

APPENDIX A: COMPUTATIONAL METHODS

Below we present in detail the methods used to perform the computations that give rise to the figures in the results section.

1. Lindblad master equation for the driven three-level system

For our notation and approach for modeling the CPT physics in a driven three-level system, we directly follow Ref. [20]. The dynamics of the Λ system in Fig. 1(a) is governed by the Hamiltonian (in the rotating frame)

$$H_\Lambda = \frac{\hbar}{2}\begin{pmatrix} -2\delta & 0 & -\Omega_1^* \\ 0 & 2\delta & -\Omega_2^* \\ -\Omega_1 & -\Omega_2 & -2\Delta \end{pmatrix}. \tag{A1}$$

The equation of motion for the density matrix ρ_Λ that describes this electronic system as an open system with relaxation and decoherence is

$$\dot{\rho}_\Lambda = \frac{-i}{\hbar}[H_\Lambda, \rho_\Lambda] + \sum_{i,j}\left(L_{ij}\rho_\Lambda L_{ij}^\dagger - \frac{1}{2}\{L_{ij}^\dagger L_{ij}, \rho_\Lambda\}\right) \tag{A2}$$

(elements ρ_{ij} are density matrix elements of ρ_Λ). Here, the Lindblad operators are defined by

$$L_{ij} = \alpha_{ij}\,|i\rangle\langle j|\,, \tag{A3}$$

$$\alpha = \frac{1}{2}\begin{pmatrix} \gamma_s & 2\Gamma_s & 2\Gamma_3 \\ 2\Gamma_s & \gamma_s & 2\Gamma_3 \\ 0 & 0 & \gamma_3 \end{pmatrix}. \tag{A4}$$

The matrix α contains all decay and decoherence rates of the system: spin flip rate Γ_s, excited-state decay rate Γ_3, spin decoherence rate γ_s, and excited-state decoherence rate γ_3.

2. Fermi contact hyperfine interaction

We consider the case where the hyperfine interaction between the Λ system and the nuclear spin is dominated by the Fermi contact interaction for the ground-state electron. This interaction is described by the Hamiltonian

$$H_f = \frac{4}{3}\mu_0\mu_B\sum_i A_i \boldsymbol{I}_i \cdot \boldsymbol{S}, \tag{A5}$$

where $A_i = \hbar\gamma_i|\psi_e(\boldsymbol{r}_i)|^2$. The gyromagnetic factor, γ_i, and the electron wave function at the position of a nucleus, $\psi_e(\boldsymbol{r}_i)$, characterize the interaction strength with the ith nuclear spin. The spin operators are defined to have eigenvalues $m_J = -J, \ldots, J$ for any spin quantum number J. This interaction term may be viewed in the form of a Zeeman interaction, $H = -\boldsymbol{\mu}\cdot\boldsymbol{B}_n$, with $\boldsymbol{\mu} = -g\mu_B\boldsymbol{S}$ the electron spin magnetic moment. The effective magnetic field due to the nuclei acting on the electron is then

$$\boldsymbol{B}_n = \frac{4}{3g}\mu_0\sum_i A_i\boldsymbol{I}_i. \tag{A6}$$

In an external magnetic field it is convenient to expand the $\boldsymbol{I}\cdot\boldsymbol{S}$ product using ladder operators. The total Hamiltonian becomes

$$H = H_z + H_f, \tag{A7}$$

$$H_z = \hbar\omega_z S_z + \sum_i \hbar\omega_i I_{i,z}, \tag{A8}$$

$$H_f = \frac{2}{3}\mu_0\mu_B\sum_i A_i(2I_{i,z}S_z + I_{i,+}S_- + I_{i,-}S_+). \tag{A9}$$

Equation (A8) represents the Zeeman energy of the electron spin and the nuclear spins in an external magnetic field applied along $\hat{\mathbf{z}}$. The first term within the summation in Eq. (A9) adds to the external field an effective magnetic (Overhauser) field $B_{n,z}$. To calculate its expectation value $\langle B_{n,z}\rangle = \mathrm{Tr}(B_{n,z}\rho_n)$, where ρ_n is the reduced density matrix comprising the nuclear spin state, it is in principle required to know the interaction strengths for all nuclei. In the case of GaAs this is well studied and $\langle B_{n,z}\rangle \approx \langle I_z\rangle \times 3.53$ T [41], and the maximum field is $B_{\max} = 5.30$ T. The Overhauser field $B_{n,z}$ translates to the Overhauser shift δ used in the results section according to $\delta = \frac{1}{2}g\mu_B B_{n,z}/\hbar$. This yields $\delta_{\max} = 16.3$ GHz. To describe DNP we use a so-called box model [4] where the electron couples equally to a number of N nuclear spins. This amounts to the change $\sum_i A_i \to A\sum_{i=1}^N$ with A the average interaction strength per nucleus. In our calculations we approximate GaAs by choosing $N = 10^5$.

The constant K in Eq. (2) is

$$K = \frac{4\mu_0\mu_B}{3\hbar}\sum_i A_i\frac{I_i^2 + I_i}{S^2 + S}. \tag{A10}$$

For GaAs, $I_i = 3/2$ for all nuclei. So $K = 10\delta_{\max}/3 = 54.3$ GHz.

3. Hyperfine relaxation rate

The cross relaxation between the electron spin and the nuclear spins is facilitated by a modulation of the hyperfine coupling due to random jumps in the electron spin state. These jumps occur on average after a correlation time τ_c. The relaxation rate is then the product of the average hyperfine coupling, the fraction of time the electron is present (f_e), and the spectral density of the electron spin fluctuations [4,42],

$$\Gamma_h = \left(\frac{A}{N\hbar}\right)^2 2f_e\frac{\tau_c}{1 + (\omega_z + \delta)^2\tau_c^2}. \tag{A11}$$

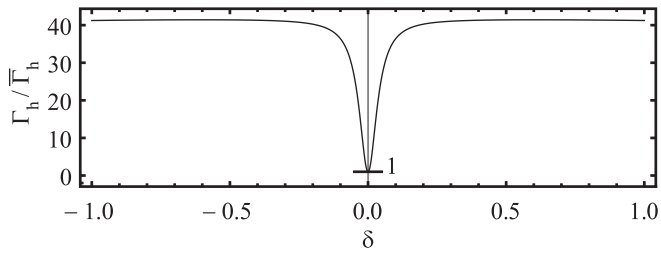

FIG. 5. Modulation of the hyperfine relaxation rate Γ_h by the Overhauser shift δ under conditions of two-laser driving. Detuning $\Delta = 1$; parameters $\Omega_{1,2}$, Γ_s, γ_s, Γ_3, γ_3 are as in Fig. 1. This graph has been used for the calculations for Figs. 2–4.

The relaxation process of the $\hat{\mathbf{z}}$ projection of the nuclear spin is allowed due to jumps in the perpendicular component of $\mathbf{S}$. For the undriven electron spin τ_c equals $T_2 = 1/\gamma_s$, i.e., the intrinsic decoherence time of the electron spin. Under conditions of laser driving τ_c is reduced when the laser driving leads to repeated excitation and spontaneous emission. The sharp variation of absorption around CPT has to be taken into account in our model. To deal with this we assume that we operate under conditions where $\omega_z \gg \delta$ and $\omega_z \gg 1/\tau_c$ so that the spectral density is approximately proportional to the inverse correlation time:

$$\frac{\tau_c}{1+(\omega_z+\delta)^2\tau_c^2} \approx \frac{1}{\omega_z^2\,\tau_c}. \tag{A12}$$

In addition, we take the inverse correlation time to be enhanced by the amount of optical transitions that disturb the electron spin state, i.e., $1/\tau_c = (\rho_{11}+\rho_{22})\gamma_s + \rho_{33}\Gamma_e$, where we obtain the ρ_{ii} from the Λ system model. For the undriven spin ρ_{33} is zero and $1/\tau_c = \gamma_s$, whereas for the driven electron spin the last term $\rho_{33}\Gamma_e$ represents the interruption of coherent spin dynamics by absorption and spontaneous emission. Around $\delta = 0$, ρ_{33} varies strongly with δ.

In our simulations we specify a value for $\overline{\Gamma}_h/\Gamma_d$ (this value is reported in the captions of Figs. 2–4) where $\overline{\Gamma}_h$ is the hyperfine relaxation rate of the equilibrium system (no laser driving). This provides the basis for the effective value of Γ_h, for which we can calculate its dependence on δ through τ_c. How this dependence controls a modulation of the effective value for $\Gamma_h/\overline{\Gamma}_h$ near CPT conditions is presented in Fig. 5 for a specific set of optical driving parameters (see caption).

4. Steady-state solution to the Fokker-Planck equation

A steady-state ($\dot{P} = 0$) solution to Eq. (3) is

$$P_{ss}(\delta) = \eta \exp\left[-\int_0^{\delta} f_1(x)/f_2(x)dx\right],$$

where

$$f_1(x) = -\dot{\delta}(x) + \delta_{\max}^2 \frac{\partial}{\partial x}[\Gamma_d + \Gamma_h(x)]/N,$$

$$f_2(x) = \delta_{\max}^2[\Gamma_d + \Gamma_h(x)]/N,$$

and η is a number that is fixed by the normalization condition $\int P(\delta)d\delta = 1$. A special solution arises in the case when $f_1(x) = ax$ and $f_2(x) = b$ with a, b constant. Then the steady-state distribution is Gaussian with standard deviation $\sigma = (b/a)^{1/2}$.

5. Electron spin dephasing from hyperfine interaction with a nuclear spin bath

Because of the slow dynamics of the nuclear spins compared to the electron spin, each measurement on the electron spin is subject to an Overhauser field $B_{n,z}$ sampled from a distribution. For example, at thermal equilibrium at the high temperatures that we consider (for nuclear spins), this is a Gaussian distribution with mean $\langle B_{n,z}\rangle = 0$ and standard deviation σ_B. For a measurement on an ensemble of electron spins (or many separate single-spin measurements), one will observe inhomogeneous dephasing as a function of time t. This can be parametrized with a function $C(t)$ that evolves from no dephasing to complete dephasing on a scale from 1 to 0:

$$C(t) = \left|\int_{-\infty}^{+\infty} P(B)\,\exp\left(-\frac{ig\mu_B Bt}{\hbar}\right)dB\right|. \tag{A13}$$

Here $P(B)$ is the probability distribution for the total field $B = B_{\text{ext}} + B_{n,z}$ (where B_{ext} is the externally applied magnetic field), taken over an ensemble of electrons. This expression captures the gradual loss of information about S_x and S_y as a function of time. For the Gaussian distribution at thermal equilibrium

$$\overline{P}(B) = \frac{1}{\sqrt{2\pi\sigma_B^2}}\,\exp\left(-\frac{B^2}{2\sigma_B^2}\right). \tag{A14}$$

The dephasing timescale T_2^* is defined as the time where Eq. (A13) reduces to $1/e$. For the Gaussian distribution $\overline{P}(B)$, Eq. (A13) yields $C(t)$ in the form $\exp[-(t/T_2^*)^2]$ with the inhomogeneous dephasing time

$$T_2^* = \frac{\sqrt{2}\hbar}{|g|\mu_B\sigma_B}. \tag{A15}$$

The steady-state distributions obtained from the feedback model with nonlinear response are not Gaussian; for those no simple expression for T_2^* is available. We define T_2^* as the time at which $C(t)$ has dropped to $1/e$ of its initial value, which is obtained by numerical evaluation of Eq. (A13). Further, it is straightforward to calculate with this definition a value for T_2^* for any of the distributions $P(\delta)$ that is presented in the results section (using $\delta = \frac{1}{2}g\mu_B B_{n,z}/\hbar$).

APPENDIX B: SIGN OF ELECTRON SPIN POLARIZATION NEAR THE CPT RESONANCE

To understand the sign changes in the spin population, as depicted in Fig. 1(c) of the main text, we revert to a model of minimum complexity that retains the essential physics for the electron spin polarization: As in the main text, we consider equal Rabi frequencies, Ω, and additionally we let the only coupling to the environment take place via Γ_3 (spontaneous decay from $|3\rangle$ to $|1\rangle$ and $|2\rangle$). All other rates in Eq. (7) are set to zero. This reduces the expression for the steady-state spin

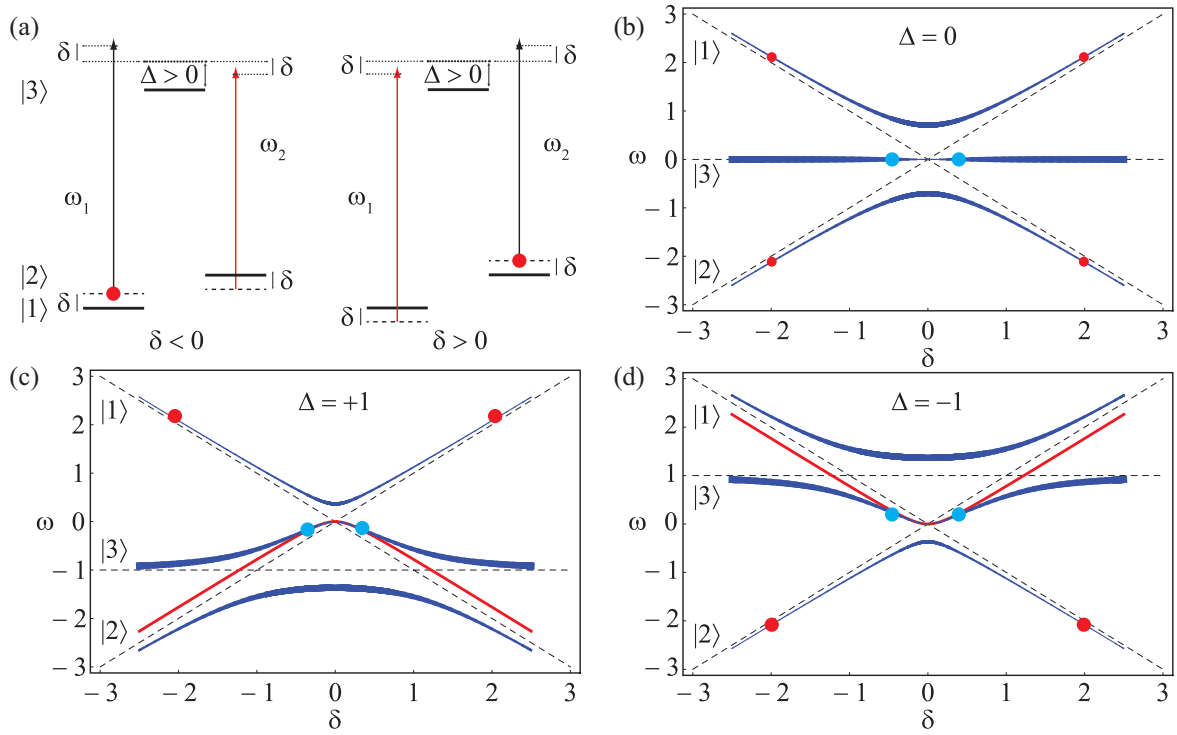

FIG. 6. (a) Optical pumping for the case $\Delta > 0$. Depending on the sign of δ the population is transferred to either of the spin states, indicated by the red dot, by the near-resonant laser (red arrow). (b)–(d) Eigenstates of H_Λ. Dashed lines represent the bare eigenstates (lasers off) and solid blue lines represent the dressed eigenstates (lasers on at $\Omega_1 = \Omega_2 = 1$). The thickness of the solid lines in (b)–(d) is proportional to the corresponding projection on $|3\rangle$. Dots indicate where the population resides. Red dots in (c) indicate the optical pumping configuration as do the red dots in (a). The blue dots show the counterintuitive population transfer near two-photon resonance. Red lines in (c) and (d) result from a two-level approximation of the Λ system.

population to

$$\langle S_z \rangle = \frac{\rho_{22} - \rho_{11}}{2} = \frac{\delta\Delta(2\delta^2 + \Omega^2)}{2[\Omega^4 + (\Omega^2 + \Delta^2 + {\Gamma_3}^2 + \delta^2)\delta^2]}, \tag{B1}$$

which has zeros at $\delta = 0$ and $\delta = \pm\Omega/\sqrt{2}$. (Incidentally, these $\delta = \pm\Omega/\sqrt{2}$ provide an approximation for the stable points depicted in Fig. 2 where $\Omega = 0.5$ and hence $\delta \approx \pm 0.35$.) These points separate the optical orientation process into two regimes, which can each be intuitively understood.

For $|\delta| > \Omega/\sqrt{2}$ the system experiences optical pumping, as depicted in Fig. 6(a). Both lasers couple their corresponding spin state to the excited state $|3\rangle$, but in the presence of nonzero Δ their detunings are not equal. The spin state that is addressed with the near-resonant laser is pumped empty, as expected. Another way to look at this, which paves the way for the explanation in the next paragraph, is as follows: Coupling mediated by the laser fields has the effect that the otherwise stable states $|1\rangle$ and $|2\rangle$ become contaminated by the decaying state $|3\rangle$, rendering them instable. This effect is stronger for the laser closest to resonance. Generally the steady state of the system tends to avoid the states that suffer stronger dissipation [48]. Hence one of the lasers coupling stronger (depicted in red) leads to transfer of spin population to the opposite spin state (where the red dot indicates the majority population).

For $|\delta| < \Omega/\sqrt{2}$ the sign of the spin population is opposite to the former case and its explanation more subtle. In order to explain we examine visually (the analytical expressions are quite involved and therefore not suited to give insight in the physics) the eigenstates of the Hamiltonian in Eq. (A1). Its characteristic equation is

$$\lambda^3 + \Delta\lambda^2 - \left(\delta^2 + \frac{|\Omega|^2}{2}\right)\lambda - \delta^2\Delta = 0, \tag{B2}$$

whose solutions are the energy eigenstates of the system coupled to the fields, depicted in Figs. 6(b)–6(d) (blue lines) as functions of δ. The corresponding eigenvectors are the dressed states of the system, which are linear combinations of $\{|1\rangle, |2\rangle, |3\rangle\}$. The thickness of each line indicates the projection of the state on $|3\rangle$. It is a measure for the dissipative character of the dressed states, since dissipation only occurs from $|3\rangle$. Again, in the steady state (after an initial transient response of a few optical cycles) population predominantly resides in the most stable (i.e., least dissipative) state. The dark state, which is free of dissipation, is in each graph at the point (0,0) (narrow portion of the middle eigenstate). The dashed lines indicate the energy of the bare states; actually they are $|1, n, m\rangle$, $|3, n-1, m\rangle$, and $|2, n-1, m+1\rangle$ where the last two variables indicate the number of laser photons of frequency ω_1 and ω_2, respectively. We chose the zero energy

to be at the midpoint of $|1\rangle$ and $|2\rangle$, such that $|1\rangle$ ($|2\rangle$) has a slope of -1 ($+1$) in the diagram. As $|\delta|$ increases beyond Δ both lasers detune far from resonance and the dressed states asymptotically approach the bare energy levels. By inspection we can now see how the spin population evolves with the detunings. First, we recognize the optical pumping as described in panel (a): In panel (c) ($\Delta > 0$) the red dots indicate that for $|\delta| \gg \Omega/\sqrt{2}$ the population resides in the upper energy eigenstate, which approaches $|1\rangle$ for $\delta < 0$ and $|2\rangle$ for $\delta > 0$; hence these dots correspond to those in panel (a). In panel (d) ($\Delta < 0$) this situation is inverted and in panel (b) the effect is absent (the smaller red dots indicate an equal division over states $|1\rangle$ and $|2\rangle$) because of the symmetric detuning. Focusing on panel (c) we study the situation near two-photon resonance: for $\delta < \Omega/\sqrt{2}$ the middle eigenstate is still the least dissipative, even though it is not a perfect dark state for nonzero δ. The population resides in this state (as indicated by the blue dots) which bends towards $|1\rangle$ for $\delta > 0$ and towards $|2\rangle$ for $\delta < 0$; in panels (b) and (d) it can be seen that this effect is inverted for $\Delta < 0$ and absent for $\Delta = 0$. The counterintuitive spin population thus arises from a combination of dark-state trapping by destructive quantum interference and the light shifts of the system.

More information on how these light shifts due to the laser fields lead to population transfer in this regime can be gained by making a two-level approximation via the method of adiabatic elimination [49]. This neglects any excitation to $|3\rangle$ and allows the system to be described by the Hamiltonian

$$H_{\text{two-level}} = \hbar \begin{pmatrix} -\delta + \frac{|\Omega|^2}{4\Delta} & \frac{|\Omega|^2}{4\Delta} \\ \frac{|\Omega|^2}{4\Delta} & \delta + \frac{|\Omega|^2}{4\Delta} \end{pmatrix}. \tag{B3}$$

This two-level approximation can be viewed as follows: In the absence of absorption, the ground-state levels acquire a Stark shift of $|\Omega|^2/4\Delta$ from the lasers, in the same direction. As a second-order effect, there is a coupling between $|1\rangle$ and $|2\rangle$ with effective Rabi frequency $|\Omega|^2/4\Delta$. This Raman coupling, corresponding to absorption and stimulated emission of the laser photons, causes an additional Autler-Townes type of splitting. The levels repel each other and the eigenstates are symmetric and antisymmetric linear combinations of $|1\rangle$ and $|2\rangle$, resulting in the energy eigenvalues $\lambda_\pm = (|\Omega|^2 \pm \sqrt{16\Delta^2\delta^2 + |\Omega|^4})/4\Delta$. Out of these λ_- is the antisymmetric, dark state. (The symmetric state λ_+ is not a dark state and hence is not a good approximation to the other eigenstate of the three-level system; unless Ω is very low or Δ very large, we disregard it here.) This approximation is plotted as the red line and agrees well with the three-level description for small δ. Additionally, it can be insightful to treat the spin-selective light shifts as an effective magnetic field acting on the system; such a description can be found in [26].

[1] M. Gaudin, J. Phys. **37**, 1087 (1976).
[2] G. Lampel, Phys. Rev. Lett. **20**, 491 (1968).
[3] S. W. Brown, T. A. Kennedy, D. Gammon, and E. S. Snow, Phys. Rev. B **54**, R17339 (1996).
[4] B. Urbaszek, X. Marie, T. Amand, O. Krebs, P. Voisin, P. Maletinsky, A. Högele, and A. Imamoglu, Rev. Mod. Phys. **85**, 79 (2013).
[5] W. A. Coish, J. Fischer, and D. Loss, Phys. Rev. B **81**, 165315 (2010).
[6] E. Barnes, L. Cywiński, and S. Das Sarma, Phys. Rev. Lett. **109**, 140403 (2012).
[7] W. A. Coish and D. Loss, Phys. Rev. B **70**, 195340 (2004).
[8] A. Greilich, A. Shabaev, D. R. Yakovlev, A. L. Efros, I. A. Yugova, D. Reuter, A. D. Wieck, and M. Bayer, Science **317**, 1896 (2007).
[9] D. J. Reilly, J. M. Taylor, J. R. Petta, C. M. Marcus, M. P. Hanson, and A. C. Gossard, Science **321**, 817 (2008).
[10] C. Latta, A. Högele, Y. Zhao, A. Vamivakas, P. Maletinsky, M. Kroner, J. Dreiser, I. Carusotto, A. Badolato, D. Schuh *et al.*, Nat. Phys. **5**, 758 (2009).
[11] I. T. Vink, K. C. Nowack, F. H. L. Koppens, J. Danon, Y. V. Nazarov, and L. M. K. Vandersypen, Nat. Phys. **5**, 764 (2009).
[12] X. Xu, W. Yao, B. Sun, D. G. Steel, A. S. Bracker, D. Gammon, and L. J. Sham, Nature (London) **459**, 1105 (2009).
[13] H. Bluhm, S. Foletti, D. Mahalu, V. Umansky, and A. Yacoby, Phys. Rev. Lett. **105**, 216803 (2010).
[14] T. D. Ladd, D. Press, K. De Greve, P. L. McMahon, B. Friess, C. Schneider, M. Kamp, S. Höfling, A. Forchel, and Y. Yamamoto, Phys. Rev. Lett. **105**, 107401 (2010).
[15] E. Togan, Y. Chu, A. Imamoglu, and M. D. Lukin, Nature (London) **478**, 497 (2011).
[16] J. Hansom, C. H. H. Schulte, C. Le Gall, C. Matthiesen, E. Clarke, M. Hugues, J. M. Taylor, and M. Atatüre, Nat. Phys. **10**, 725 (2014).
[17] M. J. Stanley, C. Matthiesen, J. Hansom, C. Le Gall, C. H. H. Schulte, E. Clarke, and M. Atatüre, Phys. Rev. B **90**, 195305 (2014).
[18] K.-M. C. Fu, C. Santori, C. Stanley, M. C. Holland, and Y. Yamamoto, Phys. Rev. Lett. **95**, 187405 (2005).
[19] E. Arimondo and G. Orriols, Lett. Nuovo Cimento **17**, 333 (1976).
[20] M. Fleischhauer, A. Imamoglu, and J. P. Marangos, Rev. Mod. Phys. **77**, 633 (2005).
[21] A. Aspect, E. Arimondo, R. Kaiser, N. Vansteenkiste, and C. Cohen-Tannoudji, Phys. Rev. Lett. **61**, 826 (1988).
[22] G. Morigi, J. Eschner, and C. H. Keitel, Phys. Rev. Lett. **85**, 4458 (2000).
[23] C. F. Roos, D. Leibfried, A. Mundt, F. Schmidt-Kaler, J. Eschner, and R. Blatt, Phys. Rev. Lett. **85**, 5547 (2000).
[24] D. Stepanenko, G. Burkard, G. Giedke, and A. Imamoglu, Phys. Rev. Lett. **96**, 136401 (2006).
[25] M. Issler, E. M. Kessler, G. Giedke, S. Yelin, I. Cirac, M. D. Lukin, and A. Imamoglu, Phys. Rev. Lett. **105**, 267202 (2010).
[26] V. L. Korenev, Phys. Rev. B **83**, 235429 (2011).
[27] J. Danon and Y. V. Nazarov, Phys. Rev. Lett. **100**, 056603 (2008).
[28] C. G. Yale, B. B. Buckley, D. J. Christle, G. Burkard, F. J. Heremans, L. C. Bassett, and D. D. Awschalom, Proc. Natl. Acad. Sci. USA **110**, 7595 (2013).

[29] J. Fischer, W. A. Coish, D. V. Bulaev, and D. Loss, Phys. Rev. B **78**, 155329 (2008).
[30] E. Barnes and S. E. Economou, Phys. Rev. Lett. **107**, 047601 (2011).
[31] S. E. Economou and E. Barnes, Phys. Rev. B **89**, 165301 (2014).
[32] G. Sallen, S. Kunz, T. Amand, L. Bouet, T. Kuroda, T. Mano, D. Paget, O. Krebs, X. Marie, K. Sakoda *et al.*, Nat. Commun. **5**, 3268 (2014).
[33] X.-F. Shi, Phys. Rev. B **87**, 195318 (2013).
[34] W. Yang and L. J. Sham, Phys. Rev. B **85**, 235319 (2012).
[35] W. Yang and L. J. Sham, Phys. Rev. B **88**, 235304 (2013).
[36] A. V. Koudinov, I. A. Akimov, Yu. G. Kusrayev, and F. Henneberger, Phys. Rev. B **70**, 241305 (2004).
[37] R. I. Dzhioev and V. L. Korenev, Phys. Rev. Lett. **99**, 037401 (2007).
[38] A. R. Onur, J. P. de Jong, D. O'Shea, D. Reuter, A. D. Wieck, and C. H. van der Wal, Phys. Rev. B **93**, 161204(R) (2016).
[39] A. Abragam, *The Principles of Nuclear Magnetism* (Oxford University Press, London, 1961), Chap. 4, pp. 104–105.
[40] M. I. D'yakonov and V. I. Perel, Zh. Eksp. Teor. Fiz. **65**, 362 (1973) [Sov. Phys.-JETP **38**, 177 (1974)].
[41] D. Paget, G. Lampel, B. Sapoval, and V. I. Safarov, Phys. Rev. B **15**, 5780 (1977).
[42] A. Abragam, *The Principles of Nuclear Magnetism* (Oxford University Press, London, 1961), Chap. 8, p. 311.
[43] A. Abragam, *The Principles of Nuclear Magnetism* (Oxford University Press, London, 1961), Chap. 8, pp. 272–289.
[44] M. Sladkov, A. U. Chaubal, M. P. Bakker, A. R. Onur, D. Reuter, A. D. Wieck, and C. H. van der Wal, Phys. Rev. B **82**, 121308 (2010).
[45] J. Danon, Nuclear spin effects in nanostructures, Ph.D. thesis, Delft University of Technology, 2009.
[46] C. Deng and X. Hu, Phys. Rev. B **72**, 165333 (2005).
[47] G. Éthier-Majcher, D. Gangloff, R. Stockill, E. Clarke, M. Hugues, C. Le Gall, and M. Atatüre, Phys. Rev. Lett. **119**, 130503 (2017).
[48] B. W. Shore, *The Theory of Coherent Atomic Excitation: Multilevel Atoms and Incoherence* (Wiley-VCH, 1990), Chap. 13.
[49] E. Brion, L. H. Pedersen, and K. Mølmer, J. Phys. A: Math. Theor. **40**, 1033 (2007).